X-ray spectroscopy-based structure of the Mn cluster and mechanism of photosynthetic oxygen evolution[1]

John H. Robblee[a,b], **Roehl M. Cinco**[a,b], and **Vittal K. Yachandra**[a,*]

[a]Melvin Calvin Laboratory, Physical Biosciences Division, Lawrence Berkeley National Laboratory, Berkeley, CA 94720, USA

[b]Department of Chemistry, University of California, Berkeley, CA 94720, USA

Abstract

The mechanism by which the Mn-containing oxygen evolving complex (OEC) produces oxygen from water has been of great interest for over 40 years. This review focuses on how X-ray spectroscopy has provided important information about the structure of this Mn complex and its intermediates, or S-states, in the water oxidation cycle. X-ray absorption near-edge structure spectroscopy and high-resolution Mn Kβ X-ray emission spectroscopy experiments have identified the oxidation states of the Mn in the OEC in each of the intermediate S-states, while extended X-ray absorption fine structure experiments have shown that 2.7 Å Mn–Mn di-μ-oxo and 3.3 Å Mn–Mn mono-μ-oxo motifs are present in the OEC. X-ray spectroscopy has also been used to probe the two essential cofactors in the OEC, Ca^{2+} and Cl^-, and has shown that Ca^{2+} is an integral component of the OEC and is proximal to Mn. In addition, dichroism studies on oriented PS II membranes have provided angular information about the Mn–Mn and Mn–Ca vectors. Based on these X-ray spectroscopy data, refined models for the structure of the OEC and a mechanism for oxygen evolution by the OEC are presented.

Keywords

Photosystem II; Oxygen evolving complex; Extended X-ray absorption fine structure; X-ray absorption near-edge structure; Electron paramagnetic resonance; S-states; Oxygen evolution; X-ray emission spectroscopy

1. Introduction

The oxidation of H_2O to O_2 by the Mn-containing oxygen evolving complex (OEC) in the chloroplasts [1], and the reduction of O_2 to H_2O by cytochrome *c* oxidase in the mitochondria [2] form the important cycle of dioxygen metabolism that is essential to both plant and animal life on earth (Eq. 1).

$$2H_2O \rightleftharpoons O_2 + 4e^- + 4H^+ \quad (1)$$
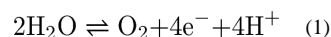
Oxygen is relatively abundant in the atmosphere primarily because of its constant regeneration by photosynthetic water oxidation by the OEC. The OEC of the photosynthetic apparatus that catalyzes the forward reaction shown in Eq. 1 contains a cluster of four Mn

---

[1]We dedicate this review to the memory of Mel Klein, our colleague, collaborator, mentor, and dear friend.

[*]Corresponding author. Fax: +1-510-486-6059; vkyachandra@lbl.gov.

atoms (reviewed in [1,3–5]). In addition to Mn, Cl^- and Ca^{2+} are essential cofactors that are required for activity [6,7]. The OEC cycles through a series of five intermediate states, S_i (i =0–4), where i represents the number of oxidizing equivalents stored on the OEC. This process is driven by the energy of four successive photons absorbed by the pigment P_{680} of the photosystem II (PS II) reaction center [8]. The Mn complex in the OEC couples the four-electron oxidation of water with the one-electron photochemistry occurring at the PS II reaction center by acting as the locus of charge accumulation (Fig. 1).

The critical questions related to this water oxidation process are the structure of the Mn complex and its nuclearity, that is the number of Mn atoms that are directly connected by bridging ligands, the oxidation state and structural changes in the Mn complex as the OEC proceeds through the S-state cycle, the structural and functional roles of the essential cofactors Ca^{2+} and Cl^-, and the mechanism by which four electrons are removed from two water molecules by the Mn complex to produce an O_2 molecule.

Mn X-ray spectroscopy studies provide direct information on the structure of the Mn cluster and on the oxidation states of the Mn atoms in the S_0, S_1, S_2 and S_3 states of the OEC. X-ray absorption spectroscopy (XAS) does not require a long-range order; the structural studies can be performed on frozen solutions. Several of the intermediate states mentioned above can be stabilized as frozen solutions. Because of the complexity of the system and the presence of many pigment and other electron-transfer components (chlorophylls, cytochromes, quinones), study of the Mn complex by optical and other spectroscopic methods can be difficult. The specificity of the XAS technique allows us to look at Mn without interference from the pigment molecules, the protein and membrane matrix, or other metals like Ca, Mg, Cu and Fe, which are also present in active preparations. X-ray K-edge spectra and Kβ X-ray emission spectra provide information about oxidation states and the site symmetry of the Mn complex, and extended X-ray absorption fine structure (EXAFS) at the K-edge furnishes information about the number, type and distances to neighboring ligand atoms (reviewed in [9–12]). Few other spectroscopic techniques provide such specificity for studying the structure of Mn in the OEC.

In this review, we present our view of the structure of the Mn cluster, which is refined based on new data, and a mechanism for water oxidation that emphasizes the recent results from our laboratory.

2. Oxidation states of Mn vs. S-states of the OEC

A key question for the understanding of photosynthetic water oxidation is whether the four oxidizing equivalents are accumulated on the four Mn ions of the OEC, or whether some ligand-centered oxidations take place before the formation and release of molecular oxygen. It is crucial to understand this problem, because the Mn redox states form the basis for any mechanistic proposal for photosynthetic water oxidation.

A promising approach to study the Mn oxidation states in the native S-states is to step samples through the S-state cycle by the application of saturating single-turnover flashes and to characterize these samples by X-ray spectroscopy. Roelofs et al. [13] reported X-ray absorption near-edge structure (XANES) data from samples in the S_0 through S_3 states produced under these physiologically relevant conditions. The flash-advanced PS II samples prepared from spinach exhibited XANES spectra that showed Mn oxidation from S_0 to S_1 and from S_1 to S_2, but no further oxidation during the S_2 to S_3 transition. These results are consistent with our earlier studies of samples that were prepared by illumination at low temperature [14,15] or by chemical treatment by Guiles et al. [16,17].

Other spectroscopic techniques such as proton relaxation enhancement [18], electron paramagnetic resonance (EPR) [19–21], UV absorption [22,23] and oxidized tyrosine D (Y_D^{ox}) EPR/spin echo [24] spectroscopies show that, in PS II, the $S_0 \rightarrow S_1$ and $S_1 \rightarrow S_2$ transitions are Mn-centered oxidations, and most groups agree that Mn redox states in the S_1 state are (III$_2$, IV$_2$) which are oxidized to (III, IV$_3$) in the S_2 state [25]. There is, however, disagreement as to whether a Mn- or ligand-centered oxidation occurs in the $S_2 \rightarrow S_3$ transition [26,27].

To resolve the controversy, we initiated high-resolution Mn Kβ X-ray emission spectroscopy (XES) studies in collaboration with Prof. Steve Cramer, who has constructed a state-of-the-art high-resolution emission spectrometer that operates at the Mn Kβ fluorescence energy and has demonstrated the feasibility of determining the oxidation states of Mn [28]. We have now completed a comprehensive Mn Kβ XES study in conjunction with XANES, a repetition of our earlier studies by Roelofs et al. [13], on sets of samples prepared in a similar manner to address the question of the oxidation states of Mn in the various S-states.

Because the actual S-state composition is of critical importance to the interpretation of the results, we characterized the samples by EPR spectroscopy, using the S_2 multiline EPR signal (MLS) as a direct measure for the S_2 state population in our samples. It is essential to obtain high concentrations of PS II in the various S-states to obtain EPR, XANES and Kβ XES data with a good signal-to-noise ratio. A Nd-YAG laser system (Spectra-Physics PRO 230-10, 800 mJ/pulse at 532 nm, 9 ns pulse width) was used to illuminate PS II samples from both sides simultaneously. Because the pulse widths of the laser are narrow compared to those of a flash lamp, double hits become negligible. The damping of the oscillation pattern is decreased, thus making it possible to derive an unique set of spectra by deconvolution. When the system becomes scrambled by frequent misses and double hits, the deconvoluted spectra are not unique. Also, the laser setup has allowed us to double the sample concentration used in earlier studies [13]. The relative S-state populations in samples given 0, 1, 2, 3, 4, 5 or 6 flashes were determined from fitting the flash-induced EPR multiline signal oscillation pattern to the Kok model, which describes S-state dephasing as a function of flash number, for each of the samples used in the X-ray spectroscopy experiments.

2.1. Mn XANES

The Mn K-edge spectra of samples given 0, 1, 2, or 3 flashes are combined with EPR information to calculate the pure S-state edge spectra. The shifts in inflection point energy positions and changes in shape are determined by second derivatives of the K-edge spectra. In addition to the shift in edge position, the $S_0 \rightarrow S_1$ (2.1 eV) and $S_1 \rightarrow S_2$ (1.1 eV) transitions are accompanied by characteristic changes in the shape of the edge, also indicative of Mn oxidation [25]. The edge position shifts very little (0.3 eV) for the $S_2 \rightarrow S_3$ transition, and the edge shape shows only minor changes [29,30]. These recent results con- firm our earlier data by Roelofs et al. [13].

2.2. Mn Kβ X-ray emission spectroscopy

High-resolution Mn Kβ X-ray emission spectroscopy has been performed on samples prepared by using 0, 1, 2, or 3 high-power laser flashes. In this technique, the energy of the Mn Kβ emission (3p$\rightarrow$1s) is measured with a high-resolution dispersive spectrometer [31]. The shape and energy of the Kβ$_{1,3}$ emission reflect the oxidation state(s) of the emitting Mn atom(s). The emission occurs from a 3p level that is mainly influenced by the number of unpaired 3d electrons and is less sensitive to the symmetry and bonding than the K-edge absorption (see below), which involves transitions to the 4p level [10]. The spin of the unpaired 3d valence electrons can be either parallel (Kβ′) or antiparallel (Kβ$_{1,3}$) to the hole

in the 3p level. The splitting between the $K\beta'$ and $K\beta_{1,3}$ peaks becomes smaller for higher oxidation states because fewer 3d electrons interact with the 3p hole. Thus, in contrast to the inflection points of the XANES edges, the $K\beta_{1,3}$ peaks shift to lower energy with higher oxidation states (Fig. 2).

Using a first-moment analysis, the position of the main $K\beta_{1,3}$ peak has been calculated for each S-state. Based on the shifts, or lack thereof, of the first moments, we concluded that Mn is not oxidized during the $S_2 \rightarrow S_3$ transition. Our results show a shift in energy between the S_0 and S_1 state spectra and between the S_1 and S_2 state, however, there is very little change between the S_2 and S_3 states.

We have used two independent X-ray spectroscopic techniques, $K\beta$ XES and XANES spectroscopy, along with EPR, to examine the Mn redox states in PS II. Fig. 3 summarizes the oscillation patterns of the XANES spectra inflection point energies (A) and of the first moments from the $K\beta_{1,3}$ spectra (B). Both patterns show large shifts between the 0-flash and 1-flash samples, which reflect the Mn-centered oxidation during the $S_1 \rightarrow S_2$ transition. A much smaller shift occurs between 1-flash and 2-flash samples, which is inconsistent with a Mn-centered oxidation during the $S_2 \rightarrow S_3$ transition. Second derivatives of the S-state XANES spectra and $K\beta$ difference spectra confirm this conclusion. We conclude that no direct Mn oxidation is involved in the $S_2 \rightarrow S_3$ transition. The proposed Mn oxidation state assignments are as follows: S_0 (II, III, IV, IV) or (III, III, III, IV); S_1 (III, III, IV, IV); S_2 (III, IV, IV, IV); S_3 (III, IV, IV, IV) and are summarized in Fig. 1 (J. Messinger, J.H. Robblee, U. Bergmann, personal communication).

Support for this conclusion has come from XANES and $K\beta$ XES studies of two-model compounds in which Mn oxidation occurs without ligand rearrangement or replacement. Of particular interest are the complexes [Mn^{III}–O–Mn^{III}]L_2 (L =N,N-bis-(2-pyridylmethyl)-N'-salicylidene-1,2-diaminoethane), poised in the Mn^{III}/Mn^{III}, Mn^{III}/Mn^{IV} and Mn^{IV}/Mn^{IV} states, and [Mn^{III}–O_2–Mn^{IV}]L_4 (L =bipy), poised in the Mn^{III}/Mn^{IV} and Mn^{IV}/Mn^{IV} states, by low-temperature preparative scale electrolysis [32]. The data show the expected shift in the K-edge and $K\beta$ XES first moments when Mn is oxidized from (III$_2$) to (III,IV) and to (IV$_2$) (H. Visser, personal communication). The $K\beta$ XES first-moment shifts of this set of complexes have been compared to the first-moment shift for the $S_1 \rightarrow S_2$ transition, taking into account the fact that the models oxidize one Mn out of two in each step, while PS II oxidizes maximally one Mn out of four. This comparison shows that the first-moment shift in the model complexes, where Mn(III) is oxidized to Mn(IV), is comparable to that seen during the $S_1 \rightarrow S_2$ transition in PS II. Most interestingly, the difference spectra for the (III$_2$) to (III,IV) or (III,IV) to (IV$_2$) transition in the mono-μ-oxo bridged complex, or the (III,IV) to (IV$_2$) transition in the di-μ-oxo bridged complex, are almost identical. This provides conclusive evidence that $K\beta$ X-ray emission spectra are less sensitive to structural changes and are predominantly determined by oxidation states of Mn, as indicated above. Thus we conclude that the lack of a change in the $K\beta$ X-ray emission spectrum for the $S_2 \rightarrow S_3$ transition is firm evidence for lack of Mn oxidation.

The critical issue is the distribution of the oxidizing equivalents in the S_3 state. In our interpretation, the oxidizing equivalent in the S_3 state is stored not on Mn, but elsewhere, probably on a ligand or protein residue. We propose that it is stored on the bridging oxo ligand (vide infra) and hypothesize that changes in the Mn K-edge and $K\beta$ X-ray emission spectra during the S_2 to S_3 transition are small, because the Mn 1s level is not perturbed as much by ligand oxidation as it is when Mn is oxidized.

3. Topological structure of the Mn cluster

XAS results that showed the existence of the 2.7-Å Mn–Mn distance [33–35] and the discovery of the MLS from the S_2 state [19,36] established the multinuclear nature of the Mn cluster. The interplay between the two methods has played an essential role in our present understanding of the structure of the Mn complex and the mechanism of water oxidation.

3.1. Mn EXAFS-based structure

The quantitation of the Fourier peak at 2.7 Å in the S_1 and S_2 states leads to 1–1.5 Mn–Mn vectors per Mn in PS II at that distance [25,37–39]. The 2.7-Å Mn–Mn distance is characteristic of di-μ-oxo bridged models, therefore it was proposed that the Mn complex in the OEC is a structure with minimally two di-μ-oxo bridges. This conclusion was based principally on the observation of the 2.7-Å Mn–Mn distance, but it was also supported by the presence of a short Mn–O distance at about 1.8 Å, which is characteristic of bridging Mn–oxo distances in multinuclear Mn complexes [40].

The Fourier transforms (FTs) from the S_1 and S_2 states also exhibit a peak at 3.3 Å that corresponds to at least one Mn–Mn interaction and a Mn–Ca interaction (see below). A Mn–Mn 3.3 Å-distance is characteristic of mono-μ-oxo-bridged Mn complexes; hence, we proposed that the Mn cluster in the OEC consists of at least one such mono-μ-oxo bridge between two Mn atoms.

Given that there are four Mn atoms in the OEC, win at least two Mn–Mn di-μ-oxo bridges and at least one Mn–Mn mono-μ-oxo bridge, it becomes physically impossible not to have a tetranuclear Mn cluster. By comparison with the structural motifs present in multinuclear Mn complexes [41,42], we proposed that the Mn cluster in PS II consists of a pair of di-μ-oxo bridged Mn binuclear clusters linked through a mono-μ-oxo bridge. There are several topological alternatives for arranging four Mn atoms that satisfy the two requirements listed above and the details are discussed in DeRose et al. [40]. Fig. 4 shows the various options that are compatible with EXAFS data and, among those options, A, E, F, G and K are especially favored.

EPR and ENDOR simulations of the MLS by Britt and coworkers [43] and Kusunoki and coworkers [44] are in better agreement with E, F or G shown in Fig. 4. Temperature dependence studies of the $g = 4.1$ S_2 signal have led Å hrling et al. [45] to propose two non-magnetically interacting Mn dimers like those shown in Fig. 4C.

It is important to emphasize that the spatial arrangement of the four Mn atoms associated with the water-oxidation complex is not definitively known. Although option A in [40] (Fig. 4A) has been used as a working model [25], the other options E, F, G or K in Fig. 4 are equally feasible, as we emphasized in DeRose et al. [40]. The mechanism proposed on the basis of density functional calculations [46] prefers option F in Fig. 4, where the two di-μ-oxo units are adjacent to each other; a structural arrangement that can more easily explain the lengthening of both of the two 2.7-Å Mn–Mn distances in the S_3 state.

3.2. Structural insights from the dichroism of the Mn cluster

PS II preparations [47,48] are membrane fragments, thus the cofactors are vectorially arranged. We have taken advantage of this to investigate the angles between the various Mn–Mn or Mn–Ca(Sr) or Mn–Cl(Br) vectors to derive geometrical information about the Mn cluster, something that is normally not available from XAS studies.

The dichroism studies have provided crucial information about the symmetry, or the lack of it, of the Mn complex that, along with the structural information described above, place constraints on the structural alternatives that are possible. The two Mn–Mn vectors at 2.7 Å are aligned at an average angle of $60\pm7°$ to the membrane normal and the 3.3-Å Mn–Mn vector is aligned at ~62° with respect to the membrane normal (vide infra). The pronounced dichroism of the Mn–Mn vectors provides evidence that the Mn cluster is asymmetric, a result that unequivocally rules out all highly symmetric structures.

4. Structural role of cofactors of the Mn cluster

4.1. Calcium cofactor

Along with Mn and Cl^-, Ca^{2+} is an essential cofactor in oxygen evolution [1,6]. Depleting this cofactor suppresses OEC activity, which can be restored (up to 90%) by replenishing with Ca^{2+}. Partial reactivation (up to 40%) results from addition of strontium to Ca-depleted PS II membranes [49,50] and no other metal ions (except VO^{2+}, vanadyl ion [51]) can restore activity [52–54].

Although Sr^{2+} replenishes the Ca-depleted centers to a similar extent as added Ca^{2+}, the slower kinetics of the OEC turnover yields an overall lower steady-state rate (40%) at saturating light intensities [55]. Substitution of Ca^{2+} with Sr^{2+} also alters the EPR multiline signal (MLS) from the S_2 state, giving narrower hyperfine splitting and different intensity patterns [50,56–58]. Most researchers addressing the stoichiometry of the Ca^{2+} cofactor in PS II now conclude that functional water oxidase activity requires one Ca^{2+}, which can be removed by low-pH/citrate or 1.2 M NaCl wash [52,59–62]. In higher plants, another more tightly bound Ca^{2+} is associated with the light-harvesting complex (LHC II) and requires harsher treatments for its removal [63–65].

There is debate about the environment of the Ca^{2+} cofactor binding site and its function. Several investigations have involved substitution of various metals into this binding site, followed by EXAFS studies on the Mn cluster. One set of experiments using EXAFS on Sr-reactivated PS II membranes was interpreted to indicate a 3.4–3.5-Å distance between the Ca (Sr) and the Mn cluster [66]. This conclusion was based on the observation of increased amplitude in the FT peak at 3.3 Å upon replacement of Ca^{2+} with Sr^{2+}, which is a heavier atom and thus a better X-ray scatterer. This close link is also supported by FTIR spectroscopic work [67] that is consistent with a carboxylate bridge between Mn and Ca. Analysis of EXAFS spectra from purified PS II membrane preparations by MacLachlan et al. also support the proximity of Ca to Mn [38]. Ca^{2+}-depletion by NaCl-washing of PS II membranes removed the 16- and 23-kDa extrinsic proteins [68] and led to a reduced amplitude for this Fourier transform peak [69]. Because of the lower X-ray scattering ability of sodium, this result was interpreted as possible Na^+ substitution for Ca^{2+} [69].

However, another Mn EXAFS study [70] did not detect any changes in the Fourier peak at 3.3 Å when Ca was replaced with Sr^{2+} or Dy^{3+} in PS II reaction center complexes lacking the 16- and 23-kDa extrinsic polypeptides. These authors found no evidence of an EXAFS-detectable Mn–Ca interaction at about 3.3 Å and proposed that Ca^{2+} was located at a distance beyond 4 Å from the Mn cluster, coordinated by a ligated water molecule to a di-μ-oxo oxygen bridge. More support came from EPR-based experiments involving Mn^{2+} substitution in Ca-depleted (inactive) PS II membranes, which indicated that the Mn^{2+}-occupied Ca^{2+} binding site was outside the first coordination region of the catalytic cluster (beyond 4 Å) [71].

4.1.1. Strontium-reconstituted OEC—Given this uncertain situation, and to further test whether a Ca binding site is close to the Mn cluster, we decided to embark on a different

approach: to use strontium EXAFS methods to probe from the Sr cofactor point-of-view for nearby Mn within 4 Å. This is the reverse of the previously described Mn EXAFS studies that concentrated on the Mn cluster [66,70], and probed for nearby Ca^{2+} or Sr^{2+} neighbors. Several factors favor Sr^{2+} as the better cofactor for this XAS study. The X-ray energies involved (16 keV for the K-edge) are more penetrating and not significantly attenuated by air. The higher X-ray absorption cross-section and fluorescence yield of Sr relative to Ca also make the experiment practicable.

We substituted Sr^{2+} for Ca^{2+} and probed from the Sr^{2+} point of view for any nearby Mn. The EXAFS of Sr-PS II probes the local environment around the Sr^{2+} cofactor to detect any nearby Mn. We focused on the functional Sr^{2+} by removing non-essential, loosely bound Sr^{2+} in the protein environment. For comparison, an inactive sample was prepared by treating the intact PS II with hydroxylamine to disrupt the Mn cluster and to produce non-functional enzyme. Sr EXAFS results indicate major differences in phase and amplitude between the functional (intact) and non-functional (NH_2OH-treated) samples. In intact samples, the FT of the Sr EXAFS shows a peak that is missing in inactive samples. This Fourier Peak II is best simulated by two Mn neighbors at a distance of 3.5 Å. Thus, with X-ray absorption studies on Sr-reconstituted PS II, we confirm the proximity of Ca^{2+} (Sr^{2+}) cofactor to the Mn cluster and show that the active site is a Mn–Ca heteronuclear cluster [72].

As an extension of this approach, polarized Sr EXAFS studies on oriented Sr^{2+}-reactivated PS II show that this Fourier peak II is highly dichroic: within the range of angles θ, between the PS II membrane normal and the X-ray electric field vector, that were examined, the magnitude of peak II was largest at 10° and smallest at 80°. The dichroism pattern is best fit by an average angle between the Mn–Sr (and therefore Mn–Ca) vectors and the membrane normal of ~23° to the membrane normal [29,73,74].

The results further bolster the contention that Ca^{2+} (Sr^{2+}) is proximal to the Mn cluster and allows us to refine the working model of the OEC in PS II. These measurements place constraints on the kinds of structures that are possible for the Mn cluster and aid in narrowing the options available.

4.1.2. Calcium-depleted OEC—The structural consequences of Ca^{2+} depletion of PS II by treatment at pH 3.0 in the presence of citrate has been determined by Mn XAS. XANES of Ca^{2+}-depleted samples in the three modified S-states (referred to here as S′-states) reveals that there is Mn oxidation on the S_1' to S_2' transition, although no evidence of Mn oxidation was found for the S_2' to S_3' transition. These results are in keeping with results from EPR studies where it has been found that the species oxidized to give the S_3' broad radical signal [75] found in Ca^{2+}-depleted PS II is tyrosine Y_z [76–78]. EXAFS measurements of Ca^{2+}-depleted samples in the S_1', S_2', and S_3' states reveals that the Fourier peak due to scatterers at~3.3 Å from Mn is strongly diminished, consistent with our previous assignment of a Ca^{2+} scattering contribution at this distance [79]. However, even after Ca^{2+} depletion, there is still significant amplitude in the third peak, further supporting our conclusion from earlier studies that the third peak in native samples is comprised of both Mn and Ca scattering. The Mn–Mn contributions making up the second Fourier peak at ~2.7 Å are largely undisturbed by Ca^{2+}-depletion.

4.2. Chloride cofactor

The results of steady-state kinetic experiments have been interpreted to indicate a halide binding site on the Mn cluster [80]. Despite a multitude of spectroscopic studies, direct structural evidence for such a site has not yet been reported.

There is one functional Cl^- per PS II unit [81], but it is unclear whether chloride is a ligand to one of the Mn atoms in any of the five S-states. Steady-state kinetic studies indicate the presence of a halide binding site on the Mn complex [7,81,82], and activity is inhibited by some compounds which compete with the Cl^- binding site, such as fluoride [82] and primary amines [82–84]. Ono et al. [85] have shown that Cl^--depleted PS II particles in the S_2 state do not have the usual MLS but rather have a signal at $g = 4.1$, signifying that an alternative S_2 state is formed. A similar EPR signal is observed on treatment with F^-. It was found that when the OEC is in this alternative state, it can no longer advance to higher S-states. However, the EPR multiline signal is restored following illumination and subsequent addition of Cl^-. Recent studies indicate that the presence of the Cl^- is necessary only for the S_2 to S_3 and S_3 to S_0 transitions of the OEC, while the earlier steps of the cycle can proceed in its absence [86,87]. These studies indicate that Cl^- is closely associated with the structure of the OEC and the mechanism of oxygen evolution, but its detailed role is as yet unclear.

F^- perturbation of the Mn–Mn distances by treatment with F^- is one of the most direct data available that implies halide as a ligand of Mn. XAS studies of F^--inhibited samples show that one of the two 2.7-Å Mn–Mn distances is increased to ~2.8 Å, which is suggestive of F^- binding to the Mn cluster [88].

Our XAS results from isotropic samples in the S_3 state have shown that there is considerable change in the Mn–Mn distances as the system advances from the S_2 to the S_3 state [89,90]. The two 2.7- Å Mn–Mn distances in the S_2 state increase to ~2.8 and 2.9–3.0 Å in the S_3 state. With the aim of determining the relative orientation of the 2.8 and 2.9–3.0- Å Mn–Mn vectors, we initiated XAS studies of oriented S_3 state samples. The results show that the two Mn–Mn vectors are dichroic. Interestingly, perhaps because of the lengthening of the Mn–Mn vectors, a new Fourier peak is observed between the first and second Fourier peaks. Comparing this FT with that of a Mn binuclear complex with one Cl^- as a terminal ligand to a Mn atom shows that the peak corresponding to Cl backscattering in the model complex is found at approximately the same apparent distance as the new Fourier peak in the PS II samples [91]. In other model compounds, the amplitude of this peak increases as the ratio of Cl/Mn increases and the peak is absent when Cl^- is not present as a ligand. In the S_3 state sample, this peak does not fit to lower Z atoms such as C, N, or O. The fit is significantly better for Cl backscattering at ~2.2 Å. The fits for the model compound are very similar. The difference in amplitude of this Fourier peak between the S_3 sample and the model is probably due to the difference in the number of Cl^- backscatterers/Mn in the model and in PS II. It is likely that in PS II the ratio is only one Cl^- per four Mn as compared to one Cl^- per two Mn in the model compound. Dichroism studies on seven different S_3 state samples show that the Fourier peak is larger at the 10° orientation compared to the 80° orientation, which suggests that the Mn–Cl vector is more parallel to the membrane normal.

5. Refined model of the Mn/Ca/Cl heteronuclear cluster

The Mn EXAFS data clearly establish an asymmetric tetranuclear Mn cluster that can accommodate two 2.7- Å Mn–Mn vectors and one 3.3- Å Mn–Mn vector. The dichroism that is present in the Mn EXAFS data shows that the two Mn–Mn vectors at 2.7 Å are aligned at average angle of 60±7° to the membrane normal. The Sr EXAFS data and data from Ca-depleted preparations place Ca^{2+} at a distance of 3.4 Å from 1–2 Mn atoms. Cheniae and coworkers have shown that Ca^{2+} is a prerequisite for the assembly of the Mn cluster [65]. There is good evidence as described above for the inclusion of Cl^- as a ligand, at least in the S_3 state. There is also evidence for the presence of at least one histidine residue as a ligand of Mn [92]. Finally, the lack of multiple scattering features [93] in the Mn and Sr EXAFS spectra indicate that the OEC does not contain a collinear ($\theta > 150°$)

arrangement of three Mn atoms (or two Mn atoms and one Ca atom). It also excludes linear Mn–O–Mn and Mn–O–Ca moieties. A proposed model is shown in Fig. 5 [72].

Additional structural constraints have become available from the recently completed oriented Sr XAS experiments. The dichroism data from the Sr XAS experiments can be combined with the dichroism data from peak III in the Mn EXAFS data to calculate the dichroism of the 3.3- Å Mn–Mn vector. This peak III, which contains equal numbers of Mn–Mn (3.3 Å) and Mn–Ca (3.4 Å) contributions, is dichroic, with an average angle of $43\pm10°$ with respect to the membrane normal [94]. Moreover, the $43\pm10°$ estimate is a $\cos^2\varphi$-weighted average of the orientations of the Mn–Mn (3.3 Å) and the Mn–Ca vectors [95–97]. Thus, having independent knowledge from Sr EXAFS experiments that the Mn–Ca dichroism is ~23° means that the 3.3 Å Mn–Mn vector is aligned at ~62° with respect to the membrane normal. Therefore, all three Mn–Mn vectors lie at the same angle (~28°) with respect to the membrane plane. The vectors are not restricted to being collinear, because each of these vectors can lie anywhere on a cone with a defined angle with respect to the membrane normal.

Because significant angular information about Mn–Mn and Mn–Ca vectors is now available, the model shown in Fig. 5 and other topological models shown in Fig. 4 can be refined to include the presence of Ca^{2+} and take into account the new dichroism data. We have chosen to modify two options from Fig. 4: option A, where the two di-μ-oxo binuclear units are connected by a mono-μ-oxo bridge, and option F, where the two di-μ-oxo motifs are formed using a common Mn atom and the mono-μ-oxo motif is placed at the end of the trinuclear unit.

One possible modification for option A from Fig. 4 is the structure shown in Fig. 5; however, this arrangement, with the Ca^{2+} at the open end of the complex, places the Ca–Mn and 3.3-Å Mn–Mn vectors roughly parallel, which is inconsistent with the current dichroism data for these vectors. Placing the Ca^{2+} at the closed end of the complex resolves this discrepancy, and the angle between the two di-μ-oxo vectors can now be adjusted.

Fig. 6A,B shows two possibilities for this configuration of Mn and Ca atoms. These placements are reconcilable with the dichroism results from the 2.7-Å Mn–Mn, 3.3-Å Mn–Mn, and 3.4-Å Mn–Ca vectors. In addition, Ca^{2+} can be incorporated into option F from Fig. 4, which has two adjacent di-μ-oxo bridged Mn–Mn moieties which are linked to another Mn atom via a mono-μ-oxo bridge. Ca^{2+} forms an open cubane with two Mn atoms forming the other two corners. This arrangement of Ca and Mn atoms is preferred by density functional theory simulations and simulations of EPR and ENDOR data from the OEC [44,46]; a variant of this structure has been proposed by Siegbahn [46].

All three refined models shown in Fig. 6 were constructed preserving the structural motifs proposed by us earlier [40] and are variations of the original model [25,72]. In each of the models in Fig. 6, the Ca^{2+} atom is not in a plane defined by either of the di-μ-oxo bridges, thus eliminating multiple scattering effects in the EXAFS. Both of these proposed models are consistent with the current Sr and Mn XAS data; however, we have not yet tested the compatibility of our XAS data with all possible topological models, including those proposed by Kusunoki and coworkers (option G in Fig. 4 [40]) [44].

6. Structural changes of the Mn cluster in the S-states

The changes in Mn–Mn distances occurring during the S_1 to S_2 and S_3 transitions within the context of the model in option A in Fig. 4 are shown in Fig. 7. However, we emphasize that the changes in Mn–Mn distances can be illustrated as well using the other topologically viable alternatives described above.

6.1. S_1 to S_2 state transition (g=4.1 or MLS S_2 state)

The first step in the scheme is the conversion of the dark stable S_1 state to the S_2 state that is characterized by the MLS. Little change is observed in the fitting parameters for Fourier peaks II and III when the Mn cluster undergoes this transition. This step involves a Mn-centered oxidation, demonstrated by the appearance of the MLS during this transition and by our Mn K-edge and Mn Kβ XES studies [13,19,30,36]. Fourier peak II, corresponding to the averaged Mn–Mn distance in each di-μ-oxo dimanganese unit, is best fit to ~2.7 Å for both the S_1 and S_2 states [40]. EXAFS studies on oriented PS II in the S_1 and S_2 states show that there is heterogeneity in the 2.7- Å vectors, which suggests that these two binuclear species are not completely equivalent [94,95].

The inequivalence of the two di-μ-oxo-bridged Mn units becomes more evident in the S_2 state that is prepared by illumination at 130 K and characterized by the *g*=4.1 EPR signal [98]. Similar results were obtained with NH_3-treated and annealed S_2 state samples [97] and in F^--treated samples [88]. In these modified S_2 states, one of the Mn–Mn distances increases to ~2.85 Å, whereas there is very little change in the other 2.7 Å or the 3.3- Å Mn–Mn distance. With the degeneracy of the 2.7 Å lifted we were able, by studying the dichroism of the Fourier peak, to assign the relative orientation of the 2.7- and 2.85- Å vectors [97]. The scheme in Fig. 7 shows that there are paths from the MLS S_2 state that lead to two states: the S_2-*g*=4.1 state inhibited by NH_3/F^- or the S_2-oxidized tyrosine residue ($Y_Z^\bullet$) states; neither of these states can proceed to the physiologically relevant S_3 state. These states are depicted in Fig. 7 as branching away from the normal pathway leading to the S_3 state by photon absorption. However, the S_2-*g*=4.1 state generated by 820-nm illumination at 130 K [99] can proceed to an S_3 state [100].

The NH_3-treated and F^--treated samples cannot advance beyond the modified S_2 state ($S_2Y_Z^\bullet$ state). It is likely that F^- or NH_3 prevents the structural changes or oxidation of the oxo-bridge involved in the formation of the S_3 state that are necessary for proceeding beyond the S_3 state. The modification of the MLS spectra upon addition of NH_3 [101] and ESEEM studies using $^{14}NH_3$ and $^{15}NH_3$ demonstrated that NH_3 becomes a ligand of Mn [102]. The asymmetry parameter derived from ESEEM results is compatible with an amido group as a bridging ligand, either between two Mn atoms or between a Mn and a Ca atom [102].

6.2. S_2 to S_3 state transition (S_3' or native S_3 state)

Significant changes are observed in the Mn–Mn distances in the S_3 state compared to the S_1 and the S_2 states. The two 2.7-Å Mn–Mn distances that characterize the di-μ-oxo centers in the S_1 and S_2 states are lengthened to ~2.8 and 3.0 Å in the S_3 state, respectively (Fig. 7). These changes in Mn–Mn distances are interpreted as consequences of the onset of substrate water oxidation in the S_3 state. Mn-centered oxidation is evident during the $S_0 \rightarrow S_1$ and $S_1 \rightarrow S_2$ transitions. During the $S_2 \rightarrow S_3$ transition, we propose that the changes in Mn–Mn distances are the result of ligand or water oxidation, leading to the formation of an oxyl radical intermediate at a bridging or terminal position. The reaction of the oxyl radical with OH^-, H_2O, or an oxo group during the subsequent S-state conversion then forms the O–O bond [90]. We propose that substrate/water oxidation occurring at this transition provides the trigger for the formation of the O–O bond; the critical step in the water oxidation reaction.

The results from isotropic S_3 samples are supported by polarized EXAFS studies on oriented PS II in the native S_3 state. The data confirm that the two di-μ-oxo-bridged Mn–Mn dimer units are not equivalent. Fourier peak II of S_3 is dichroic and is readily resolved to Mn–Mn distances of ~2.8 Å and ~3.0 Å, each with its own distinct projection on the membrane

normal [91]. The polarized EXAFS data are different from those observed in the S_2 state which showed two Mn–Mn distances at ~2.7 Å [94,97].

The other unproductive state generated from the S_2-MLS state is denoted in Fig. 7 as the $S_2Y_Z^\bullet$ state (referred to as the S_3' state below) generated in Ca-depleted samples. The Ca-depleted samples are inactive in O_2 evolution, while a broad g=2 EPR signal has been observed in the S_3' state of such samples [75]. In such samples, the g=2 broadened EPR signal has been confirmed to arise from $Y_Z^\bullet$ [76,77,103], and it is proposed that the signal is broadened by interaction with the spin on the Mn cluster [104].

We recently reported the XAS analysis from calcium- depleted S_3' state samples [79]. The position of Peak II in the FT of S_3' state samples was invariant relative to that of the native S_2 state sample. The EXAFS fits showed that the 2.7- Å Mn–Mn distances did not lengthen as observed in the native S_3 state samples and are essentially unchanged from those of the native S_2 state. This finding is surprising because the Mn K-edges from these Ca-depleted samples showed a behavior similar to the native PS II in that little or no shift was observed in the $S_2' \rightarrow S_3'$ transition. This difference between the native S_3 and calcium-depleted S_3' states indicates that the core di-μ-oxo-bridged structure is probably dissimilar in the native S_3 and the S_3' states, with the structure in the S_3' state resembling the native S_2 state structure. It is reasonable to question how the transfer of one electron from the Mn cluster onto Y_Z can result in major changes in the Mn–Mn distances, as is observed in the native S_3 state. The roles of Y_Z and the Mn cluster in the process of water oxidation are clearly delineated by the comparison of the S_3 and the S_3' states. Instead of the Mn cluster simply providing a scaffold for water oxidation, this comparison shows that the structural change in the Mn cluster initiated by the transfer of an electron from the Mn cluster to Tyr_Z during the $S_2 \rightarrow S_3$ transition may provide the trigger to the chemistry of the formation of the O–O bond. The results show that the Mn cluster is involved in a much more intimate manner in the catalysis than just providing the framework. The implications to the mechanism are significant (see below).

In Ca^{2+}-depleted systems the tyrosine Y_Z radical is stabilized, and the oxidation of the Mn–OEC and the concomitant changes in Mn–Mn distances are prevented. In the S_3 state, with Ca^{2+} present, the radical resides on the Mn cluster; however, in the absence of Ca^{2+}, the radical resides on tyrosine Z. Thus, Ca^{2+} is proposed to play a crucial role in controlling the redox potential and thus the course of the mechanism of water oxidation.

6.3. S_0 to S_1 state transition

A comparison of the EXAFS spectra from the S_0 and S_1 states has been completed [30]. The most prominent change is the decrease in the amplitude of the 2.7- Å feature in the S_0 sample. This is consistent with the presence of two slightly different Mn–Mn distances around 2.7 Å. The fits show the lengthening of one Mn–Mn distance from 2.72 Å (S_1) to about 2.85 Å (S_0) and an increase in the average Mn–O/N distance. In contrast, no reasonable fits with two different Mn–Mn distances were possible for peak II in the S_1 state.

The structural changes on the S_0 to S_1 transition can be explained by the oxidation of one Mn(II) to Mn(III), because this would account for both the lengthening of the Mn–O/N bonds and of one Mn–Mn distance. The EXAFS results point, along with the XANES data, to $Mn(II,III,IV_2)$ as Mn redox states in S_0.

7. Structure-based mechanism of water oxidation

We have proposed earlier a model for the S_3 state in which an oxyl radical is generated on one of the μ-oxo-bridges, which results in an increase of one of the Mn–Mn distances to

~2.95 Å (Fig. 7) [4,90]. Consistent with our XANES results is the implication in this structure that the oxidative equivalent is not stored on the Mn atoms per se during the $S_2 \rightarrow S_3$ transition but is delocalized with significant charge and spin density on the bridging oxo ligand. Junge and coworkers have proposed a mechanism involving Mn oxidation during the $S_0 \rightarrow S_1$ and $S_1 \rightarrow S_2$ transitions, and the oxidation of bound substrate, OH^-, to a hydroxide radical during the $S_2 \rightarrow S_3$ transition, with a small admixture of a peroxide intermediate [105]. For the S_3 state, Renger and coworkers have proposed an equilibrium between bound hydroxide (or water) and peroxide bound between two Mn atoms [106].

Two essential factors are considered to construct possible structural arrangements of the Mn cluster in the S_3 state. First, our Mn K-edge inflection point data better support the interpretation that there is little or no oxidation of Mn during the $S_2 \rightarrow S_3$ transition. These data are reinforced by our recent Mn Kβ XES studies of the various S-states [30]. Second, the Mn–Mn distance in both of the di-μ-oxo-bridged units increases from 2.72 Å to 2.82 Å and 2.95 Å, upon the formation of the S_3 state. These changes imply a significant structural change in the Mn cluster as it proceeds to the S_3 state. It is difficult to rationalize such changes in Mn–Mn distance as arising purely from Mn oxidation. We propose that substrate/ water oxidation chemistry is occurring at this transition, leading to the significant structural changes

In addition to oxo-bridging ligands, Mn terminal oxo ligands have also been proposed to be involved in dioxygen formation [107,108]. It has been proposed that Mn is ligated to activated O (Mn=O) produced by the abstraction of protons from Mn-bound water by a nearby tyrosine [77,109,110], and the O–O bond is proposed to form between the oxo ligands of two adjacent Mn atoms [5]. However, it is difficult to understand how changes in terminal ligation can generate such a profound change on the Mn–Mn distances in the S_3 state as reported here. Replacement of terminal ligands in di-μ-oxo-bridged model compounds has a minimal effect on the Mn–Mn distance of 2.7 Å that is characteristic of such di-μ-oxo bridged Mn compounds [41,42].

The case for the involvement of the bridging oxygen atoms during the $S_2 \rightarrow S_3$ transition and in the mechanism of oxygen evolution is many fold. It is easy to rationalize increases in Mn–Mn distances as being due to changes in the bridging structure.

The disappearance of the multiline signal upon advancement to the S_3 state does not necessarily indicate Mn oxidation during the $S_2 \rightarrow S_3$ transition; the lack of a multiline signal is also consistent with the formation of a radical on a bridging oxygen atom, which changes the spin state of the Mn complex. Parallel-mode EPR studies by Kawamori and coworkers have shown the presence of EPR resonances at $g=12$ and 8 that are best simulated by an $S=1$ excited spin state species in the S_3 state [111]. A similar signal from the S_3 state has recently been reported by Ioannidis and Petrouleas [112]. These signals are consistent with the coupling of the $S = 1/2$ spin of the Mn complex in the S_2 state with the $S = 1/2$ radical introduced in the S_3 state.

Siegbahn and Crabtree have proposed a mechanism on the basis of quantum chemical studies where they have tried to reconcile the various biophysical data [113]. Spin state considerations led them to propose a Mn–O oxyl intermediate in the S_3 state, with radical character on the terminal oxygen ligand, with the formation of the O–O bond proposed to occur between the oxyl radical and an outer-sphere water molecule. Recent calculations by Siegbahn produced an energy minimum for the formation of the oxyl radical on the bridging O atom [46]. The Siegbahn and Crabtree mechanism involves only one Mn in the oxidation process and involves a radical species in the S_3 state as proposed by our group.

We propose that the O–Mn–O angle in one of the di-μ-oxo-bridged Mn–Mn moieties decreases in the S_3 state and as a consequence draws the two bridging oxo ligands closer for the imminent formation of an O–O bond before O_2 release. Consequently, the distance between the two Mn atoms lengthens. We previously proposed that in the S_4 state a dioxyl radical is produced which spontaneously converts to a peroxo species with the formation of an O–O bond (Fig. 8) [4]. This proposal is inspired from the study of a synthetic inorganic di-μ-oxo-bridged di-Cu compound, that has been shown to convert into an isomer with the formation of an O–O bond between the two bridged oxygens [114]. Alternatively, the formation of the oxyl radical on one dimer in the S_3 state and its reaction with OH^- or H_2O either on the other Mn dimer or in the outer sphere during the subsequent S-state conversion can lead to the formation of the O–O bond (Fig. 8). The results by Messinger and coworkers support the presence of two non-equivalent exchangeable sites in the S_3 state as required by this proposal [108,115].

Our proposed mechanism avoids the formation of the O–O bond until the most oxidized state (S_4) is reached. This precludes the formation and release of peroxide or other oxidation products of water in the earlier S-states, thus preventing the system from 'short circuiting' and avoiding the risk of damaging the polypeptides of PS II.

Acknowledgments

Abbreviations

EPR	electron paramagnetic resonance
EXAFS	extended X-ray absorption fine structure
FT	Fourier transform
MLS	multiline EPR signal
OEC	oxygen evolving complex
PS II	photosystem II
Y_D^{ox}	oxidized tyrosine D
$Y_Z^\bullet$	oxidized tyrosine residue
XANES	X-ray absorption near-edge structure
XAS	X-ray absorption spectroscopy
Kβ XES	Kβ X-ray emission spectroscopy

References

1. Debus RJ. Biochim Biophys Acta. 1992; 1102:269–352. [PubMed: 1390827]

2. Babcock GT, Wikström M. Nature Lond. 1992; 356:301–309. [PubMed: 1312679]

3. Britt, RD. Oxygenic Photosynthesis: The Light Reactions. Ort, DR.; Yocum, CF., editors. Kluwer Academic; Dordrecht: 1996. p. 137-164.

4. Yachandra VK, Sauer K, Klein MP. Chem Rev. 1996; 96:2927–2950. [PubMed: 11848846]

5. Tommos C, Babcock GT. Acc Chem Res. 1998; 31:18–25.

6. Yocum CF. Biochim Biophys Acta. 1991; 1059:1–15.

7. Yocum, CF. Manganese Redox Enzymes. Pecoraro, VL., editor. VCH; New York: 1992. p. 71-84.

8. Kok B, Forbush B, McGloin M. Photochem Photobiol. 1970; 11:457–476. [PubMed: 5456273]

9. Cramer, SP. X-ray Absorption: Principles, Applications and Techniques of EXAFS, SEXAFS, and XANES. Koningsberger, DC.; Prins, R., editors. Wiley-Interscience; New York: 1988. p. 257-320.

10. Peng G, de Groot FMF, Hämäläinen K, Moore JA, Wang X, Grush MM, Hastings JB, Siddons DP, Armstrong WH, Mullins OC, Cramer SP. J Am Chem Soc. 1994; 116:2194–2290.

11. Yachandra VK. Methods Enzymol. 1995; 246:638–675. [PubMed: 7752941]

12. Yachandra, VK.; Klein, MP. Biophysical Techniques in Photosynthesis. Amesz, J.; Hoff, AJ., editors. Kluwer Academic; Dordrecht: 1996. p. 337-354.

13. Roelofs TA, Liang W, Latimer MJ, Cinco RM, Rompel A, Andrews JC, Sauer K, Yachandra VK, Klein MP. Proc Natl Acad Sci USA. 1996; 93:3335–3340. [PubMed: 11607649]

14. Goodin DB, Yachandra VK, Britt RD, Sauer K, Klein MP. Biochim Biophys Acta. 1984; 767:209–216.

15. McDermott AE, Yachandra VK, Guiles RD, Cole JL, Dexheimer SL, Britt RD, Sauer K, Klein MP. Biochemistry. 1988; 27:4021–4031. [PubMed: 2843222]

16. Guiles RD, Zimmermann JL, McDermott AE, Yachandra VK, Cole JL, Dexheimer SL, Britt RD, Wieghardt K, Bossek U, Sauer K, Klein MP. Biochemistry. 1990; 29:471–485. [PubMed: 2154247]

17. Guiles RD, Yachandra VK, McDermott AE, Cole JL, Dexheimer SL, Britt RD, Sauer K, Klein MP. Biochemistry. 1990; 29:486–496. [PubMed: 2154248]

18. Sharp, RR. Manganese Redox Enzymes. Pecoraro, VL., editor. VCH; New York: 1992. p. 177-196.

19. Dismukes GC, Siderer Y. Proc Natl Acad Sci USA. 1981; 78:274–278. [PubMed: 16592949]

20. Messinger J, Robblee JH, Yu WO, Sauer K, Yachandra VK, Klein MP. J Am Chem Soc. 1997; 119:11349–11350.

21. Messinger J, Nugent JHA, Evans MCW. Biochemistry. 1997; 36:11055–11060. [PubMed: 9333322]

22. van Leeuwen PJ, Heimann C, van Gorkom HJ. Photosynth Res. 1993; 38:323–330. [PubMed: 24317986]

23. Dekker, JP. Manganese Redox Enzymes. Pecoraro, VL., editor. VCH; New York: 1992. p. 85-103.

24. Styring SA, Rutherford AW. Biochemistry. 1988; 27:4915–4923.

25. Yachandra VK, DeRose VJ, Latimer MJ, Mukerji I, Sauer K, Klein MP. Science. 1993; 260:675–679. [PubMed: 8480177]

26. Ono TA, Noguchi T, Inoue Y, Kusunoki M, Matsushita T, Oyanagi H. Science. 1992; 258:1335–1337. [PubMed: 17778358]

27. Iuzzolino L, Dittmer J, Dörner W, Meyer-Klaucke W, Dau H. Biochemistry. 1998; 37:17112–17119. [PubMed: 9860823]

28. Bergmann U, Grush MM, Horne CR, DeMarois P, Penner-Hahn JE, Yocum CF, Wright DW, Dubé CE, Armstrong WH, Christou G, Eppley HJ, Cramer SP. J Phys Chem B. 1998; 102:8350–8352.

29. Cinco, RM.; Fernandez, C.; Messinger, J.; Robblee, JH.; Visser, H.; McFarlane, KL.; Bergmann, U.; Glatzel, P.; Cramer, SP.; Sauer, K.; Klein, MP.; Yachandra, VK. Photosynthesis: Mechanisms and Effects. Garab, G., editor. Kluwer Academic; Dordrecht: 1998. p. 1273-1278.

30. Messinger, J.; Robblee, JH.; Fernandez, C.; Cinco, RM.; Visser, H.; Bergmann, U.; Glatzel, P.; Cramer, SP.; Campbell, KA.; Peloquin, JM.; Britt, RD.; Sauer, K.; Klein, MP.; Yachandra, VK. Photosynthesis: Mechanisms and Effects. Garab, G., editor. Kluwer Academic; Dordrecht: 1998. p. 1279-1282.

31. Bergmann, U.; Cramer, SP. SPIE Conference on Crystal and Multilayer Optics. SPIE; San Diego, CA: 1998. p. 198-209.

32. Horner O, Anxolabéhère-Mallart E, Charlot MF, Tchertanov L, Guilhem J, Mattioli TA, Boussac A, Girerd JJ. Inorg Chem. 1999; 38:1222–1232. [PubMed: 11670906]

33. Kirby JA, Robertson AS, Smith JP, Thompson AC, Cooper SR, Klein MP. J Am Chem Soc. 1981; 103:5529–5537.

34. Yachandra VK, Guiles RD, McDermott A, Britt RD, Dexheimer SL, Sauer K, Klein MP. Biochim Biophys Acta. 1986; 850:324–332.

35. Yachandra VK, Guiles RD, McDermott AE, Cole JL, Britt RD, Dexheimer SL, Sauer K, Klein MP. Biochemistry. 1987; 26:5974–5981. [PubMed: 3318924]

36. Hansson Ö, Andréasson LE. Biochim Biophys Acta. 1982; 679:261–268.

37. Penner-Hahn JE, Fronko RM, Pecoraro VL, Yocum CF, Betts SD, Bowlby NR. J Am Chem Soc. 1990; 112:2549–2557.

38. MacLachlan DJ, Hallahan BJ, Ruffle SV, Nugent JHA, Evans MCW, Strange RW, Hasnain SS. Biochem J. 1992; 285:569–576. [PubMed: 1637347]

39. Kusunoki, M.; Takano, T.; Ono, T.; Noguchi, T.; Yamaguchi, Y.; Oyanagi, H.; Inoue, Y. Photosynthesis : from Light to Biosphere. Mathis, P., editor. Kluwer Academic; Dordrecht: 1995. p. 251-254.

40. DeRose VJ, Mukerji I, Latimer MJ, Yachandra VK, Sauer K, Klein MP. J Am Chem Soc. 1994; 116:5239–5249.

41. Wieghardt K. Angew Chem Int Ed Engl. 1989; 28:1153–1172.

42. Pecoraro, VL. Manganese Redox Enzymes. VCH; New York: 1992.

43. Peloquin JM, Britt RD. Biochim Biophys Acta. 2001; 1503:96–111. [this issue]. [PubMed: 11115627]

44. Hasegawa K, Ono TA, Inoue Y, Kusunoki M. Chem Phys Lett. 1999; 300:9–19.

45. Åhrling KA, Smith PJ, Pace RJ. J Am Chem Soc. 1998; 120:13202–13214.

46. Siegbahn PEM. Inorg Chem. 2000; 39:2923–2935. [PubMed: 11232834]

47. Berthold DA, Babcock GT, Yocum CF. FEBS Lett. 1981; 134:231–234.

48. Kuwabara T, Murata N. Plant Cell Physiol. 1982; 23:533–539.

49. Ghanotakis DF, Babcock GT, Yocum CF. FEBS Lett. 1984; 167:127–130.

50. Boussac A, Rutherford AW. Biochemistry. 1988; 27:3476–3483.

51. Lockett CJ, Demetriou C, Bowden SJ, Nugent JHA. Biochim Biophys Acta. 1990; 1016:213–218.

52. Ono TA, Inoue Y. FEBS Lett. 1988; 227:147–152.

53. Ghanotakis DF, Babcock GT, Yocum CF. Biochim Biophys Acta. 1985; 809:173–180.

54. Ono TA, Inoue Y. Arch Biochem Biophys. 1989; 275:440–448. [PubMed: 2556965]

55. Boussac A, Rutherford AW. Chem Scr. 1988; 28A:123–126.

56. Boussac A, Zimmermann JL, Rutherford AW. Biochemistry. 1989; 28:8984–8989. [PubMed: 2557913]

57. Sivaraja M, Tso J, Dismukes GC. Biochemistry. 1989; 28:9459–9464. [PubMed: 2558720]

58. Tso J, Sivaraja M, Dismukes GC. Biochemistry. 1991; 30:4734–4739. [PubMed: 1851435]

59. Ädelroth P, Lindberg K, Andréasson LE. Biochemistry. 1995; 34:9021–9027. [PubMed: 7619801]

60. Cammarata KV, Cheniae GM. Plant Physiol. 1987; 84:587–595. [PubMed: 16665485]

61. Shen JR, Satoh K, Katoh S. Biochim Biophys Acta. 1988; 933:358–364.

62. Katoh, S.; Satoh, K.; Ohno, T.; Chen, J-R.; Kashino, Y. Progress in Photosynthesis Research. Biggins, J., editor. Martinus Nijhoff; Dordrecht: 1987. p. I.5.625-628.

63. Davis DJ, Gross EL. Biochim Biophys Acta. 1975; 387:557–567. [PubMed: 1138889]

64. Han KC, Katoh S. Plant Cell Physiol. 1993; 34:585–593.

65. Chen C, Kazimir J, Cheniae GM. Biochemistry. 1995; 34:13511–13526. [PubMed: 7577940]

66. Latimer MJ, DeRose VJ, Mukerji I, Yachandra VK, Sauer K, Klein MP. Biochemistry. 1995; 34:10898–10909. [PubMed: 7662671]

67. Noguchi T, Ono TA, Inoue Y. Biochim Biophys Acta. 1995; 1228:189–200.

68. Seidler A. Biochim Biophys Acta. 1996; 1277:35–60. [PubMed: 8950371]

69. MacLachlan DJ, Nugent JHA, Bratt PJ, Evans MCW. Biochim Biophys Acta. 1994; 1186:186–200.

70. Riggs-Gelasco PJ, Mei R, Ghanotakis DF, Yocum CF, Penner-Hahn JE. J Am Chem Soc. 1996; 118:2400–2410.

71. Booth PJ, Rutherford AW, Boussac A. Biochim Biophys Acta. 1996; 1277:127–134.

72. Cinco RM, Robblee JH, Rompel A, Fernandez C, Yachandra VK, Sauer K, Klein MP. J Phys Chem B. 1998; 102:8248–8256.

73. Cinco RM, Robblee JH, Rompel A, Fernandez C, Yachandra VK, Sauer K, Klein MP. J Synchrotron Rad. 1999; 6:419–420.

74. Cinco, RM. PhD Thesis. University of California; Berkeley, Berkeley, CA: 1999. LBNL Report 44 753

75. Boussac A, Zimmermann JL, Rutherford AW, Lavergne J. Nature. 1990; 347:303–306.

76. Hallahan BJ, Nugent JHA, Warden JT, Evans MCW. Biochemistry. 1992; 31:4562–4573. [PubMed: 1316150]

77. Gilchrist ML Jr, Ball JA, Randall DW, Britt RD. Proc Natl Acad Sci USA. 1995; 92:9545–9549. [PubMed: 7568170]

78. Tang XS, Randall DW, Force DA, Diner BA, Britt RD. J Am Chem Soc. 1996; 118:7638–7639.

79. Latimer MJ, DeRose VJ, Yachandra VK, Sauer K, Klein MP. J Phys Chem B. 1998; 102:8257–8265.

80. Lindberg K, Wydrzynski T, Vänngård T, Andréasson LE. FEBS Lett. 1990; 264:153–155.

81. Lindberg K, Andréasson LE. Biochemistry. 1996; 35:14259–14267. [PubMed: 8916911]

82. Sandusky PO, Yocum CF. Biochim Biophys Acta. 1986; 849:85–93.

83. Sandusky PO, Yocum CF. FEBS Lett. 1983; 162:339–343.

84. Sandusky PO, Yocum CF. Biochim Biophys Acta. 1984; 766:603–611.

85. Ono T, Zimmermann JL, Inoue Y, Rutherford AW. Biochim Biophys Acta. 1986; 851:193–201.

86. Wincencjusz H, van Gorkom HJ, Yocum CF. Biochemistry. 1997; 36:3663–3670. [PubMed: 9132019]

87. Wincencjusz H, Yocum CF, van Gorkom HJ. Biochemistry. 1999; 38:3719–3725. [PubMed: 10090760]

88. DeRose VJ, Latimer MJ, Zimmermann JL, Mukerji I, Yachandra VK, Sauer K, Klein MP. Chem Phys. 1995; 194:443–459.

89. Liang, W.; Roelofs, TA.; Olsen, GT.; Latimer, MJ.; Cinco, RM.; Rompel, A.; Sauer, K.; Yachandra, VK.; Klein, MP. Photosynthesis: From Light to Biosphere. Mathis, P., editor. Kluwer; Dordrecht: 1995. p. 413-416.

90. Liang W, Roelofs TA, Cinco RM, Rompel A, Latimer MJ, Yu WO, Sauer K, Klein MP, Yachandra VK. J Am Chem Soc. 2000; 122:3399–3412.

91. Fernandez, C.; Cinco, RM.; Robblee, JH.; Messinger, J.; Pizarro, SA.; Sauer, K.; Yachandra, VK.; Klein, MP. Photosynthesis: Mechanisms and Effects. Garab, G., editor. Kluwer Academic; Dordrecht: 1998. p. 1399-1402.

92. Tang X-S, Diner BA, Larsen BS, Gilchrist ML Jr, Lorigan GA, Britt RD. Proc Natl Acad Sci USA. 1994; 91:704–708. [PubMed: 8290585]

93. Westre TE, DiCicco A, Filipponi A, Natoli CR, Hedman B, Solomon EI, Hodgson KO. J Am Chem Soc. 1994; 116:6757–6768.

94. Mukerji I, Andrews JC, DeRose VJ, Latimer MJ, Yachandra VK, Sauer K, Klein MP. Biochemistry. 1994; 33:9712–9721. [PubMed: 8068650]

95. George GN, Prince RC, Frey TG, Cramer SP. Phys B. 1989; 158:81–83.

96. George GN, Cramer SP, Frey TG, Prince RC. Biochim Biophys Acta. 1993; 1142:240–252. [PubMed: 8386938]

97. Dau H, Andrews JC, Roelofs TA, Latimer MJ, Liang W, Yachandra VK, Sauer K, Klein MP. Biochemistry. 1995; 34:5274–5287. [PubMed: 7711049]

98. Liang W, Latimer MJ, Dau H, Roelofs TA, Yachandra VK, Sauer K, Klein MP. Biochemistry. 1994; 33:4923–4932. [PubMed: 8161553]

99. Boussac A, Girerd JJ, Rutherford AW. Biochemistry. 1996; 35:6984–6989. [PubMed: 8679522]

100. Zimmermann JL, Rutherford AW. Biochemistry. 1986; 25:4609–4615.

101. Beck WF, Brudvig GW. Biochemistry. 1986; 25:6479–6486. [PubMed: 3024709]

102. Britt RD, Zimmermann JL, Sauer K, Klein MP. J Am Chem Soc. 1989; 111:3522–3532.

103. Peloquin JM, Campbell KA, Britt RD. J Am Chem Soc. 1998; 120:6840–6841.

104. Lakshmi KV, Eaton SS, Eaton GR, Frank HA, Brudvig GW. J Phys Chem B. 1998; 102:8327–8335.

105. Haumann M, Junge W. Biochim Biophys Acta. 1999; 1411:86–91. [PubMed: 10216154]

106. Karge M, Irrgang KD, Renger G. Biochemistry. 1997; 36:8904–8913. [PubMed: 9220978]

107. Rüttinger W, Dismukes GC. Chem Rev. 1997; 97:1–24. [PubMed: 11848863]

108. Messinger J, Badger M, Wydrzynski T. Proc Natl Acad Sci USA. 1995; 92:3209–3213. [PubMed: 11607525]

109. Hoganson CW, Babcock GT. Science. 1997; 277:1953–1956. [PubMed: 9302282]

110. Pecoraro VL, Baldwin MJ, Caudle MT, Hsieh WY, Law NA. Pure Appl Chem. 1998; 70:925–929.

111. Matsukawa T, Mino H, Yoneda D, Kawamori A. Biochemistry. 1999; 38:4072–4077. [PubMed: 10194321]

112. Ioannidis N, Petrouleas V. Biochemistry. 2000; 39:5246–5254. [PubMed: 10819993]

113. Siegbahn PEM, Crabtree RH. J Am Chem Soc. 1999; 121:117–127.

114. Halfen JA, Mahapatra S, Wilkinson EC, Kaderli S, Young VG Jr, Que L Jr, Zuberbuhler AD, Tolman WB. Science. 1996; 277:1953–1956.

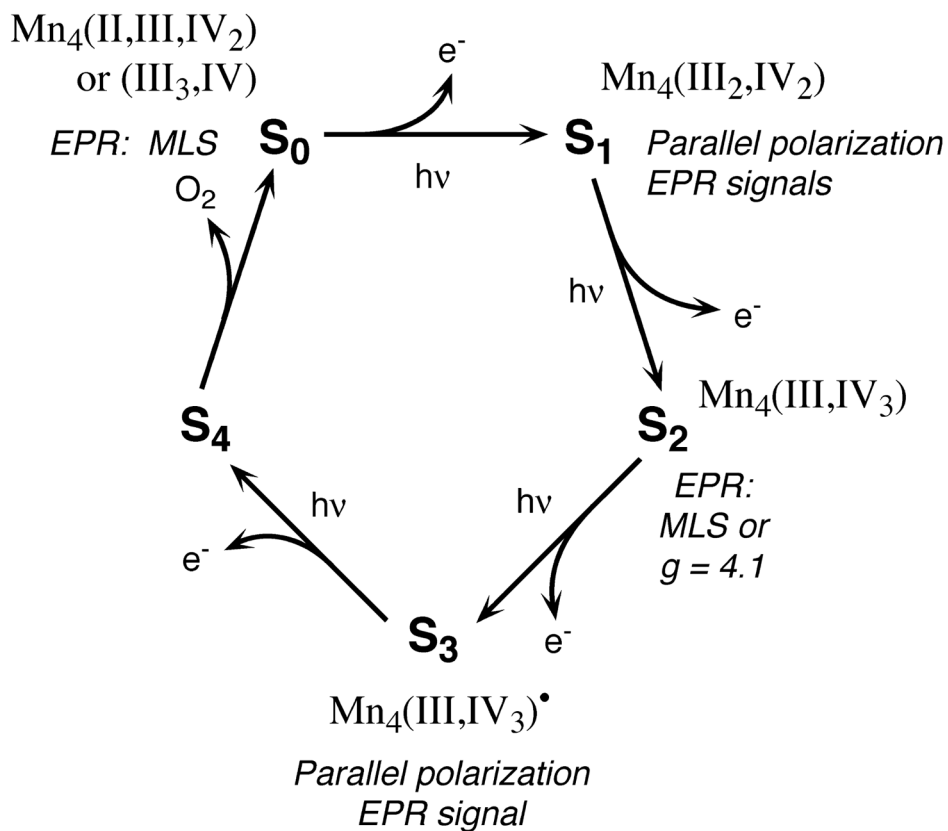115. Hillier W, Messinger J, Wydrzynski T. Biochemistry. 1998; 37:16908–16914. [PubMed: 9836583]

$Mn_4(II,III,IV_2)$
or (III_3,IV)

e-

$Mn_4(III_2,IV_2)$

EPR: MLS S_0 ⟶ S_1 *Parallel polarization EPR signals*

O_2 hν

S_4 hν   hν S_2 $Mn_4(III,IV_3)$

e-   *EPR: MLS or g = 4.1*

hν   hν

S_3 e-

$Mn_4(III,IV_3)^{\bullet}$

Parallel polarization EPR signal

Fig. 1.
The S-state scheme for oxygen evolution. Proposed Mn oxidation states and corresponding EPR signals are shown for each S-state in the Kok cycle.
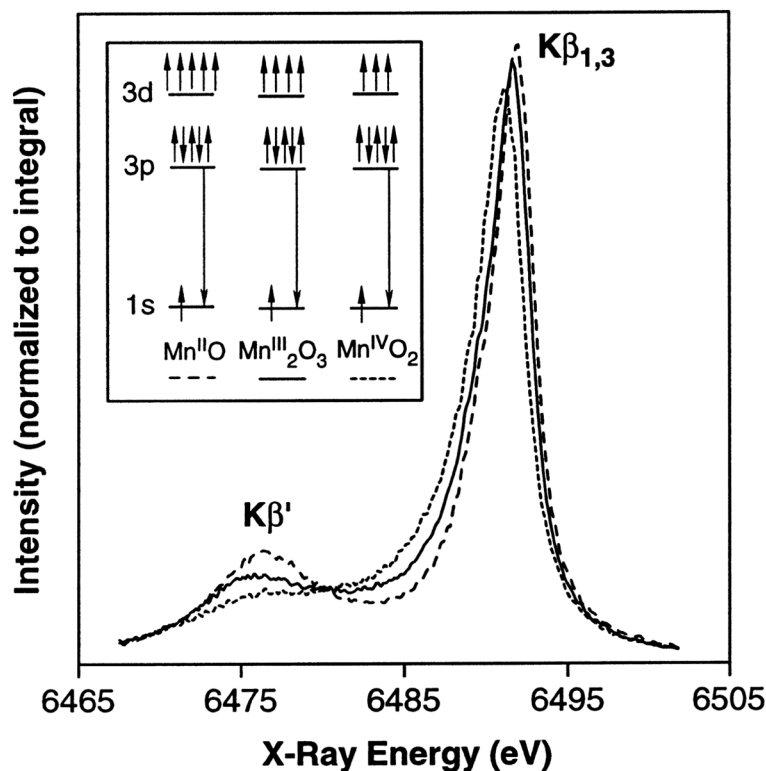
Fig. 2.
Kβ X-ray emission spectra of Mn oxides (adapted from Bergmann et al. [28]). The Kβ spectra consist of two main features: the Kβ′ peak at ~6475 eV and the $K\beta_{1,3}$ peak at ~6490 eV. The separation of these two features is due to the exchange interaction of the unpaired 3d electrons with the 3p hole, which is formed as a final state after the core hole is filled by a 3p→1s fluorescence transition. The spin of the unpaired 3d valence electrons can be either parallel (Kβ′) or antiparallel ($K\beta_{1,3}$) to the hole in the 3p level. The splitting between the Kβ′ and $K\beta_{1,3}$ peaks becomes smaller for higher oxidation states because fewer 3d electrons interact with the 3p hole. Thus, in contrast to the inflection points of the XANES edges, the $K\beta_{1,3}$ peaks shift to lower energy with higher oxidation states, as is seen above with the Mn oxides. The magnitude of the $K\beta_{1,3}$ peak first-moment shift for $Mn_2^{III}O_3 \rightarrow Mn^{IV}O_2$ is roughly a factor of four larger than the first-moment shift for the $S_1 \rightarrow S_2$ transition, where only one Mn out of four is being oxidized.
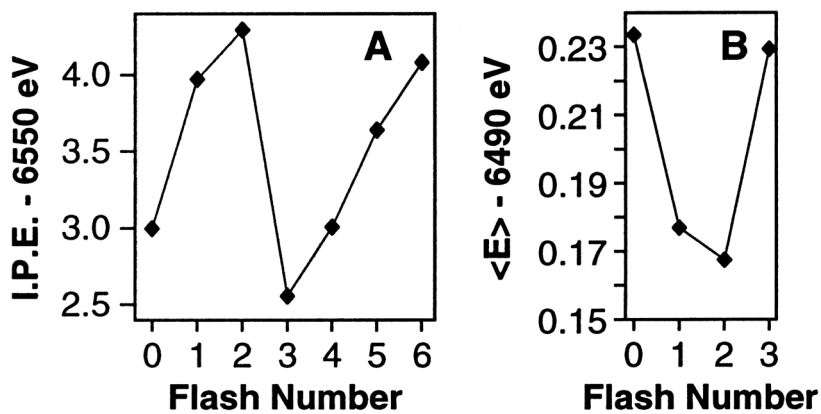
Fig. 3.
Oscillation patterns from XANES and Kβ XES flash (nF) experiments. (A) Oscillation of XANES inflection point energies (I.P.E.) of 0F to 6F samples. (B) Oscillation of first moments (<E>) of Kβ spectra from 0F to 3F samples (4F to 6F were not collected). XANES and Kβ X-ray emission spectra shift in opposite directions in response to Mn oxidation (see text for details).
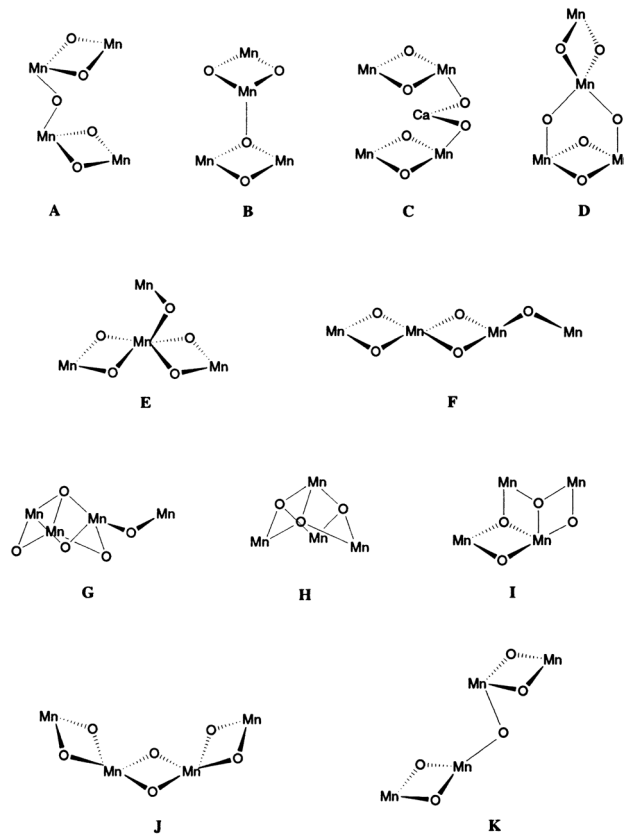
Fig. 4.
Possible core structures for the active site of the OEC in PS II. Adapted from DeRose et al. [40]. Only Mn and bridging O are shown.
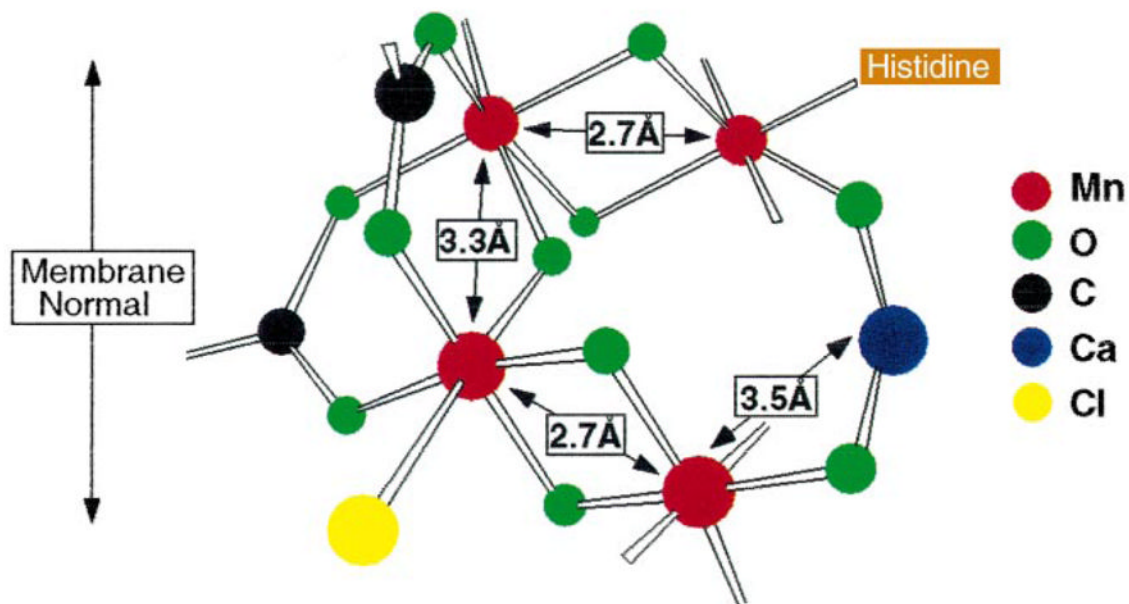
Fig. 5.
Proposed model for the active site of the OEC in PS II from the work of Cinco et al. [72]. The model incorporates the finding from the isotropic Sr-substituted PS II studies: Sr^{2+} (and therefore Ca^{2+}) is intimately linked to the Mn cluster at a distance of ~3.4–3.5 Å. This linkage requires single-atom (oxygen) bridging that can derive from acidic protein residues (aspartate or glutamate), hydroxide, or water. Depicted is one of several possible configurations consistent with the findings of the isotropic Sr EXAFS studies.
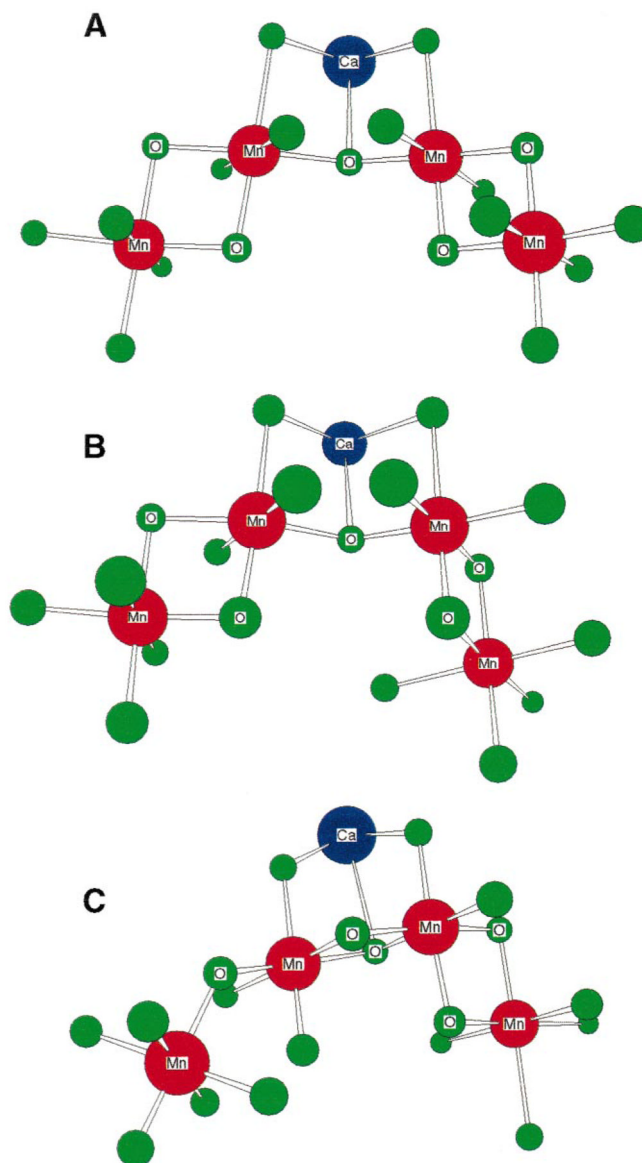
Fig. 6.
Refined models for the active site of the OEC in PS II. These models incorporate the recent finding from oriented Sr-substituted PS II studies that the Sr–Mn vectors lie at an average angle of ~23° with respect to the membrane normal; thus, the refined angle for the 3.3 Å Mn–Mn vector is ~62°. The distance between the two Mn atoms on either end of the complex in model A can be somewhat shortened by using a different oxygen ligand atom from the inner Mn to form the di-μ-oxo binuclear unit on the right side. This is shown in model B. Model C is a variation on a model originally proposed by Siegbahn [46]. The position of the Mn on the end of the mono-μ-oxo bridge can be varied by rotation about the inner Mn–O mono-μ-oxo bond.
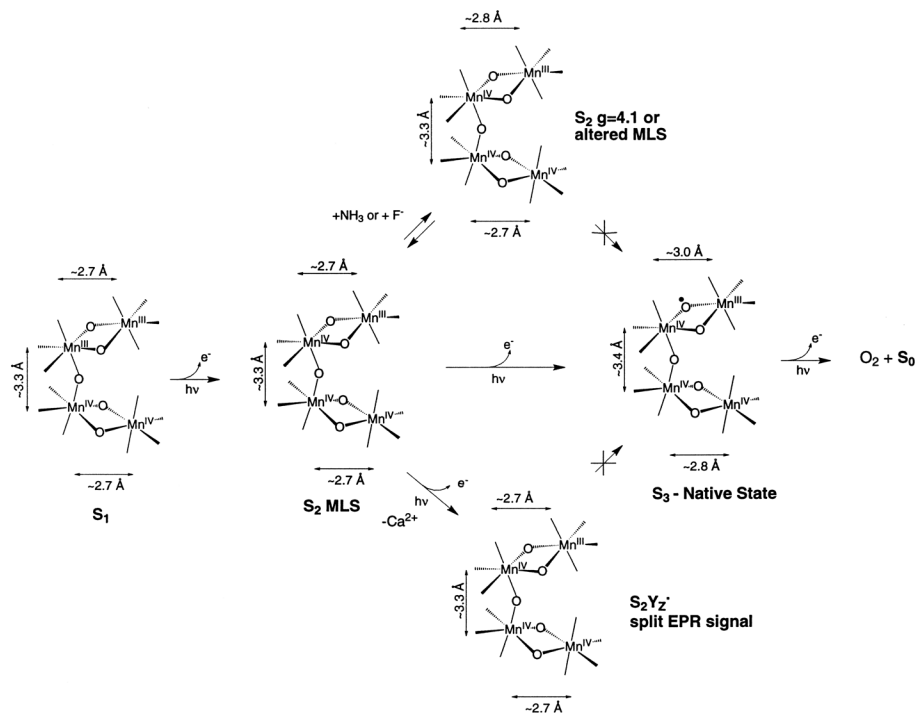
Fig. 7.
Summary of the changes in Mn–Mn distances in the native S_1, native S_2, modified S_2, $S_3{}'$ ($S_2Y_Z^\bullet$), and native S_3 states of PS II as determined by XAS. Reprinted from Liang et al. [90]. Copyright 2000 American Chemical Society
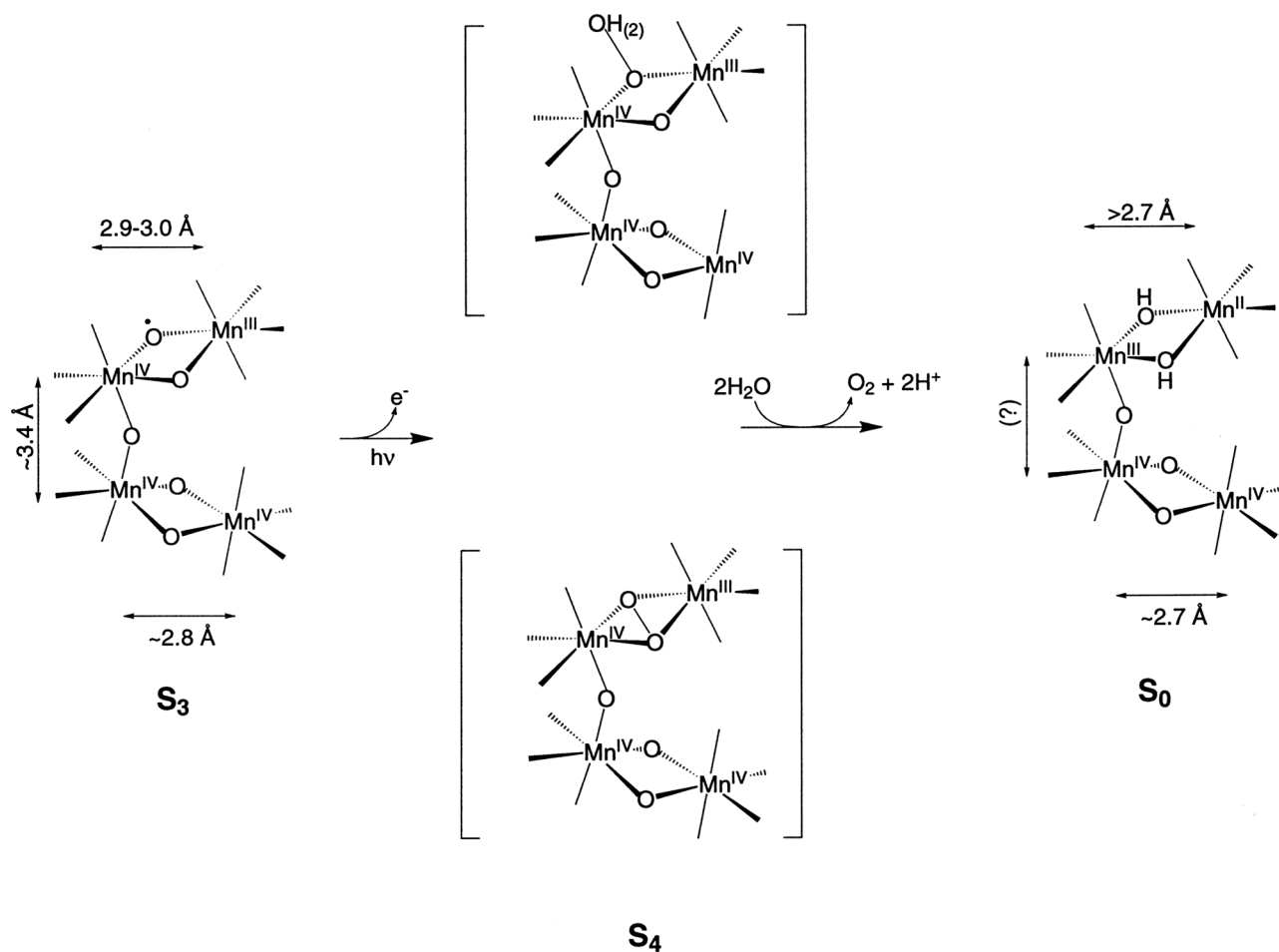
Fig. 8.
Scheme showing two different paths by which an oxyl radical formed in the S_3 state may form an O–O bond in the transient S_4 state before release of dioxygen. One path involves the formation of an O–O bond between the two oxo groups of one binuclear unit. The other path for the formation of the O–O bond is the reaction of the oxyl radical formed with OH^- or H_2O that is a ligand of Mn or in the outer sphere of the Mn cluster. The Mn–Mn distances in the transient S_4 state are unknown at present. Reprinted from Liang et al. [90]. Copyright 2000 American Chemical Society